Thermal Tides and Martian Dust Storms: Direct Evidence for Coupling

CONWAY B. LEOVY

Department of Atmospheric Sciences, University of Washington, Seattle, Washington 98195

RICHARD W. ZUREK

Jet Propulsion Laboratory, California Institute of Technology, Pasadena, California 91103

Observations of surface pressure oscillations at the Viking 1 and Viking 2 lander sites on Mars indicate that the thermally driven global atmospheric tides were closely coupled to the dust content of the Martian atmosphere, especially during northern fall and winter, when two successive global dust storms occurred. The onset of each of these global storms was marked by substantial, nearly simultaneous increases in the dust opacity and in the range of the daily surface pressure variation observed at both lander sites. Although both the diurnal and semidiurnal tidal surface pressure components were amplified at Lander 1 during the onset of a global dust storm, the semidiurnal component was greatly enhanced in relation to the diurnal tide. Semidiurnal wind components were prominent at both lander sites during the height of the global dust storm. We have attempted to interpret these observations using simplified dynamical models. In particular, the semidiurnal wind component can be successfully related to the observed surface pressure variation using a simplified model of a semidiurnally forced Ekman boundary layer. On the other hand, a classical atmospheric tidal model shows that the preferential enhancement of the semidiurnal surface pressure oscillation at Lander 1 can be produced by a tidal heating distribution which places most of the heating (per unit mass) above 10-km altitude. Furthermore, when a dust storm expands to global scale, it does so rather quickly, and the total atmospheric heating at the peak of the dust storm can represent more than 50% of the available insolation. The Viking observations suggest that a number of mechanisms are important for the generation and decay of these episodic Martian global dust storms.

INTRODUCTION

Surface pressure measurements at the Viking 1 and Viking 2 landing sites during midsummer ($L_s \sim 120°$, where L_s is the aerocentric longitude of the sun, referenced to 0° at northern vernal equinox) showed significant diurnal oscillations. *Hess et al.* [1977] have shown that these oscillations were due to the global thermal tides. The amplitude of the semidiurnal tidal pressure oscillations was used as the basis for estimating the heating amplitude, and it was concluded that some 10% of the available solar flux was taken up by the atmosphere, either by direct absorption or by convection and infrared transfer. The tidal phase suggested a heating phase lag relative to local noon such as would be produced by convective transfer from the surface, but the amplitude seemed too large to be accounted for by heat transfer from the surface alone. This unexpectedly large tidal amplitude could be understood in terms of the solar extinction and sky brightness measurements at the landers [*Pollack et al.*, 1977]. They found normal-incidence optical depths of order 0.5 and 0.4 at Landers 1 and 2 due to dust haze and were also able to show that the haze had a strongly absorbing component. *Gierasch and Goody* [1972] had suggested that even thin dust haze could be an effective heating agent in the Martian atmosphere, and this idea was supported by recent calculations of *Zurek* [1978], who used Mariner 9 data to model the optical properties of the dust. *Pollack et al.* [1979] have also shown that there was strong heating due to the dust haze at the lander sites during northern midsummer. Thus dust heating is a dynamically important process even during northern midsummer, the season of maximum atmospheric clarity [*Leovy et al.*, 1973*a*].

Since midsummer there have been large variations in optical depth at the two sites, culminating in major opacity peaks near $L_s = 205°$ and $L_s = 295°$ [*Pollack et al.*, 1979]. These were associated with discrete dust storms observed elsewhere on the planet and with planet-wide opacity increases observed by the Viking orbiter cameras and infrared thermal mapper [*Briggs et al.*, 1979; *Peterfreund and Kieffer*, 1979]. Consequently, they have been interpreted as manifestations of global dust storms, similar to those previously seen by Mariner 9 [*Masursky et al.*, 1972] and by ground-based observers [*Capen and Martin*, 1972]. *Ryan and Henry* [1979] have described the meteorological variations which accompanied these two events. In the present paper we shall show the observed relationships between the diurnal and semidiurnal tides and the global dust storms. We also present preliminary theoretical interpretations of the tidal observations and, in the last section, discuss the significance of these and other meteorological observations for global dust storm generation and decay.

DIURNAL VARIATIONS OF PRESSURE AND WIND

The time variation of optical depth measured at the two lander sites by *Pollack et al.* [1979] is compared with the two diurnal pressure ranges in Figure 1. The pressure ranges show the data-encoding digitization increment of 0.08 mbar, but it is clear that sharp jumps in diurnal pressure range at each site were coincident with the opacity jumps which occurred as dust spread over each site. The jumps in Lander 1 and Lander 2 pressure ranges and in Lander 1 opacity were essentially simultaneous. At Lander 2, large opacity fluctuations, data gaps, and complete extinction of the sun mask the simultaneity of the events, but the diurnal temperature range at Lander 2 drops sharply at the same time as the first opacity increase at Lander 1. This drop reflects the arrival of the first dust cloud at that site [*Ryan and Henry*, 1979]. It is less clear when the opacity effect of the second storm reached Lander 2. We shall show that the pressure range is primarily produced by the global tides. Hence, the simultaneity of the local opacity in-

Paper number 8B1093.
0148-0227/79/008B-1093$01.00

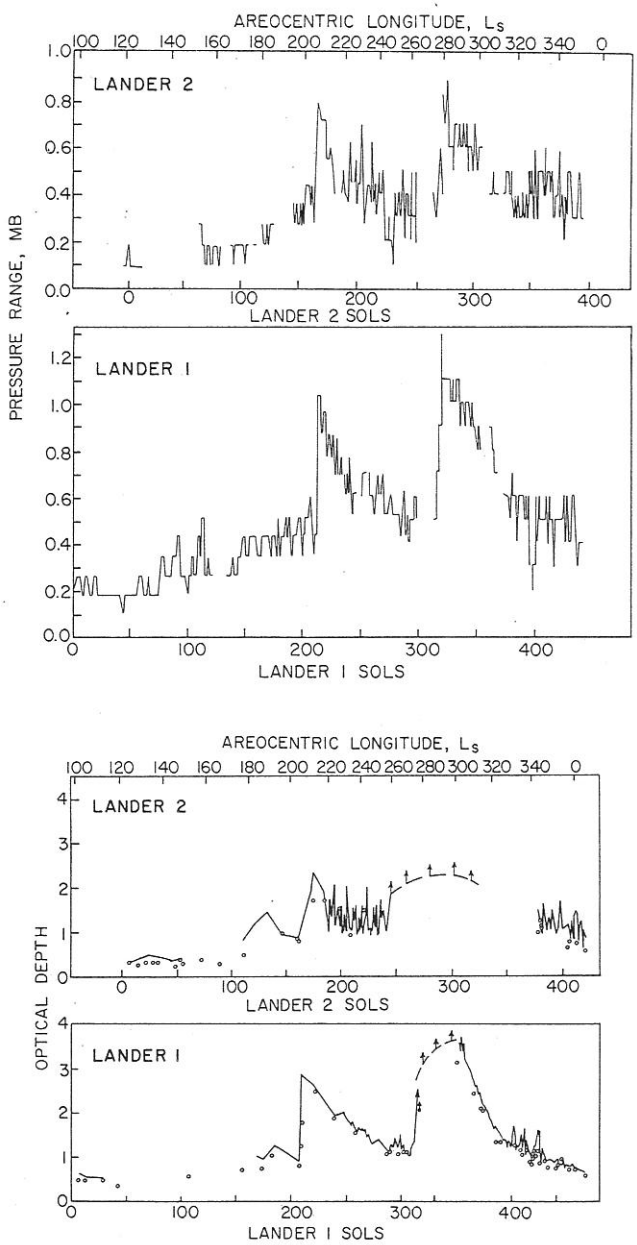

Fig. 1. (Top) Daily pressure range at the lander sites. (Bottom) Normal-incidence opacities deduced by *Pollack et al.* [1979] from solar extinction measurements taken at Lander 1 and Lander 2. Solid lines are morning measurements, circles are afternoon measurements, and dashed segments with arrows indicate periods where only lower limits can be determined.

creases and of the jumps in pressure range is striking evidence for the rapidity of the global spread of dust. The pressure ranges also track the local opacity well during the quasi-exponential decay phases of the dust storms and during the gradual rise in opacity which occurred before the onset of the first global storm. This correspondence illustrates the close coupling between atmospheric dust load and global-scale dynamical activity. It is also interesting to note that there is a suggestion of one or more minor global dynamical events in the pressure range data near Viking Lander 1 (VL 1) sol 100 ($L_s \sim 147°$), a period when there is little opacity data at the sites. (The 'sol' is the Martian solar day, 88,775 s. For convenience we divide the sol into 24 units, which we loosely term 'hours.')

Figure 2 shows diurnal wind hodographs and the corresponding pressure variation at the Viking Lander 2 site (48°N, 226°W). These have been obtained by collecting the data into 24 equal time bins each sol and averaging over 6-sol intervals. This averaging period was chosen to encompass the major periodicity in the synoptic variability, approximately 3 sols [*Ryan et al.*, 1978], to be short enough to resolve variability with respect to global dust storm onset and decay and to provide a sufficiently large number of samples in each local time bin. Typically, there are several hundred wind measurements and 20–30 pressure measurements per bin. Each wind measurement is in turn the average of 16 point samples. In Figure 2*a* the hodograph is qualitatively similar to the hodographs obtained during the midsummer period. The wind and pressure oscillations are predominantly diurnal, of relatively small amplitude, and the rotation of the wind vector is clockwise. Figure 2*b* corresponds to the period just before the onset of the first global dust storm. Pressure and wind, though somewhat irregular, show much more pronounced semidiurnal components. The hodograph has a 'two-loop' signature with a small clockwise loop between approximately 2100 and 0900 hours and a larger clockwise loop between 0900 and 2100 hours. The small loop occurs during the most stable part of the sol, when coupling to winds aloft is expected to be minimal.

Both diurnal and semidiurnal components of the pressure oscillations increase markedly after the onset of the first global storm, as do the corresponding wind oscillations (Figure 2*c*). The two-loop signature has become much more pronounced. During the decay phase of the first global storm, diurnal and semidiurnal components of the wind and pressure oscillations decrease (Figure 2*d*), but the wind oscillation remains predominantly semidiurnal. Figure 2*e* illustrates the period just after the onset of the second global dust storm. There has been a striking increase in both the diurnal and semidiurnal components of the wind oscillation, particularly the semidiurnal component. The amplitude of the pressure variation is also large, but it appears primarily as a sharp pressure surge during the late morning rather than as a clear-cut combination of a diurnal and a semidiurnal oscillation. Evidently, higher harmonics of the pressure are also important at this time. Some 30 sols later, similar wind oscillations are seen at the Viking 2 site (Figure 2*f*), although the mean wind has shifted to the northeast as a consequence of a buildup of relatively high pressure north of the site [*Ryan and Henry*, 1979]. By this time the pressure variation has regained its earlier signature, dominated by large diurnal and semidiurnal components.

Figure 3 compares daily pressure curves for Lander 1 and Lander 2 sites for various 6-sol periods. It can be seen that the pressure oscillations are larger at Lander 1 (22.5°N, 48°W) than at Lander 2 and that the sharp jumps in amplitude at dust storm onset are largely due to jumps in the semidiurnal component. Viking 1 wind speeds also jumped sharply at these times, and they had a predominantly semidiurnal variation, but there is uncertainty about wind directions at some times of day as a result of failure of the wind quadrant sensor heating filament early in the mission [*Hess et al.*, 1977]. Consequently, Lander 1 hodographs are not shown.

These features of the pressure oscillation are illustrated in Figures 4 and 5. The diurnal and semidiurnal components increase together at dust storm onset at Lander 2, but the diurnal component remains the larger of the two. On the other hand, at Lander 1 the semidiurnal component is dominant during the strong initial phases of each storm. Pressure phases (times of pressure maxima) in Figure 5 show that the diurnal

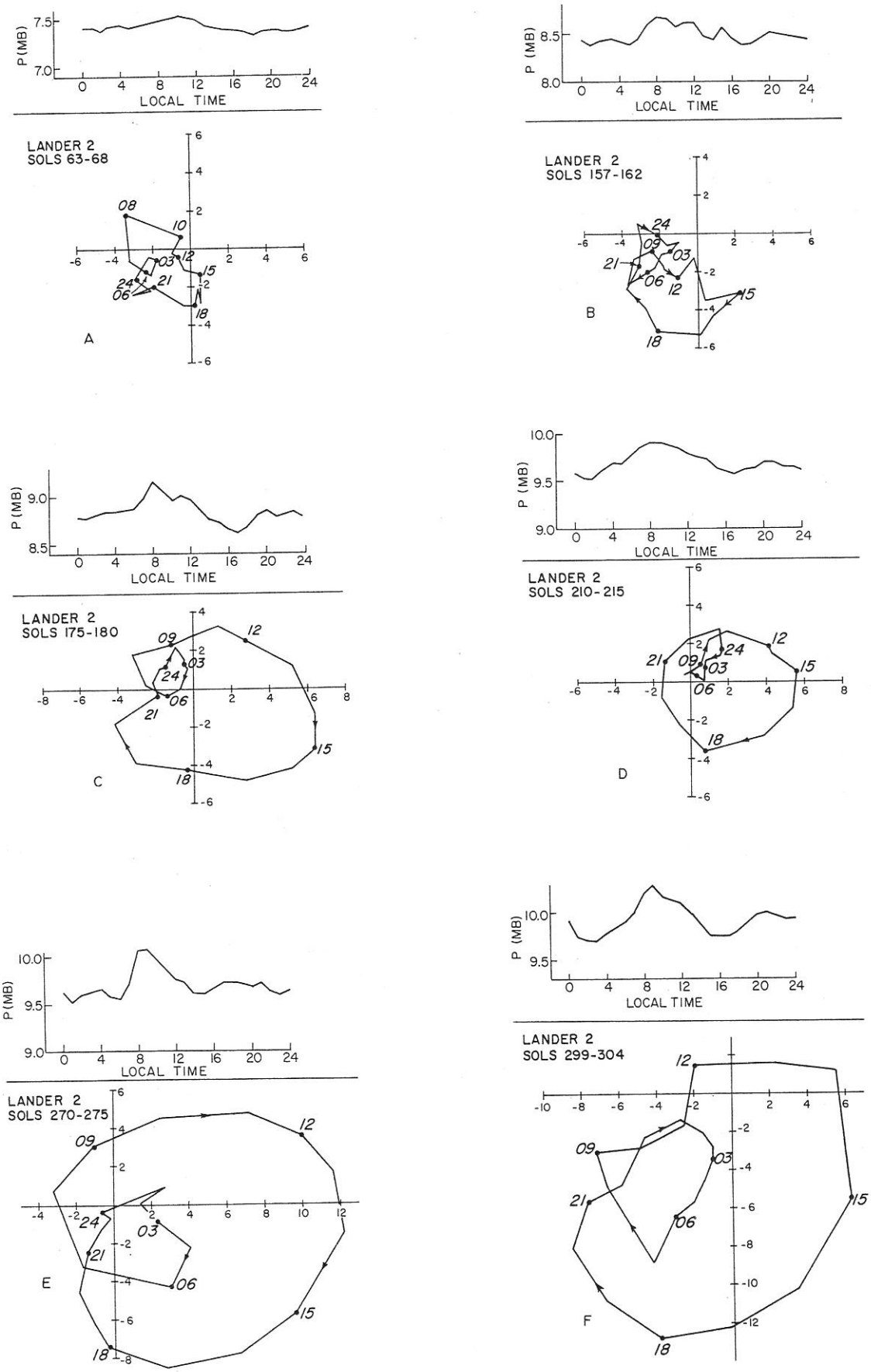

Fig. 2. (*a–f*) Wind hodographs and daily pressure curves averaged over selected periods at the Lander 2 site. Local time is expressed in Martian hours ($\frac{1}{24}$ sol), and the wind vector for a given time would be given by a line connecting the origin to the appropriate point on the hodograph curve. Further description is provided in the text.

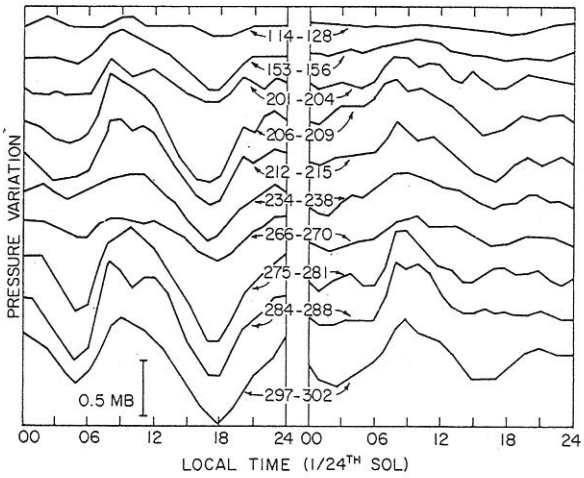

Fig. 3. Daily pressure variation at the two lander sites for selected time intervals. Lander 1 measurements are on the left, and Lander 2 on the right. Curves are identified by the areocentric longitude L_s and have been offset from one another for clarity.

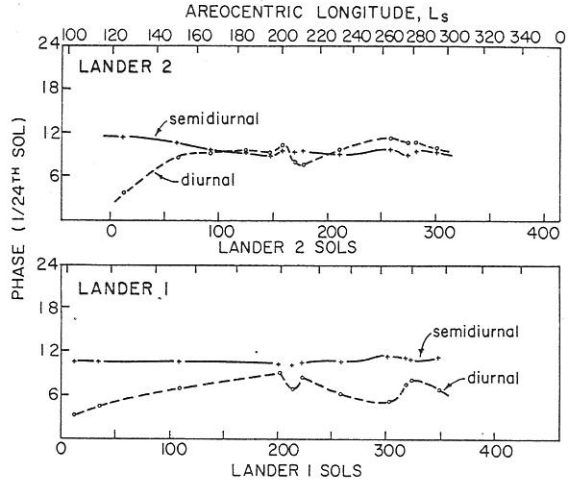

Fig. 5. Phases (expressed as hour of maximum) of the diurnal and semidiurnal pressure components. A tidal heating rate which is maximum at local noon would produce diurnal and semidiurnal pressure maxima at 0600 and 0900 hours, respectively, for an undamped atmospheric tide.

pressure oscillation reaches its maximum near or shortly before 0900 hours at both sites during the dust storms but tends to be earlier during the more dust free midsummer period, as well as between storms at Lander 1. At Lander 2 the semidiurnal oscillation reaches its maximum near 1100 hours during the relatively clear midsummer period but shifts earlier to about 0900 hours as the atmosphere becomes dustier. This shift is consistent with increasing predominance of solar absorption over convective heating as the season progresses [*Hess et al.*, 1977]. On the other hand, the peak of the semidiurnal pressure oscillation remains near 1100 hours at Lander 1 throughout the mission, and this behavior is more difficult to reconcile with classical tidal theory.

Figure 6 shows the time-dependent behavior of the wind amplitudes and phases at Lander 2. The predominance of the diurnal component of zonal wind variation during midsummer and of the semidiurnal component during the second global dust storm is illustrated. During the dusty period the semidiurnal west wind maximum leads the semidiurnal pressure maximum by approximately 5 hours, and it leads the semidiurnal south wind maximum by 3 hours. Diurnal phases are more irregular: zonal wind tends to lead the meridional wind by 6–8 hours, but the phase lead of zonal wind with respect to pressure varies from 1 to 7 hours.

Relationship Between Semidiurnal Wind and Pressure Oscillations

In order to interpret the semidiurnal winds we employ a simple model of a semidiurnally forced Ekman boundary layer. The linearized equation of motion for an oscillating wind can be written

$$(i\sigma + 2\Omega\hat{\mathbf{k}}x)\mathbf{u} = -RT\nabla(\ln p_s) + K(\partial^2\mathbf{u}/\partial z^2) \qquad (1)$$

where $\sigma = m\Omega$, the oscillation frequency, is an integer multiple of the diurnal frequency Ω, $\hat{\mathbf{k}}$ is the vertical unit vector, $\mathbf{u}$ is the complex amplitude of the wind oscillation, R is the specific gas constant, T is the local temperature, p_s is the complex amplitude of the surface pressure oscillation, K is a vertical eddy

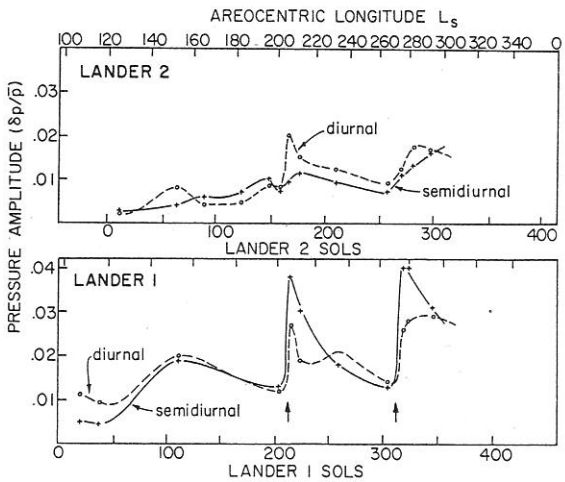

Fig. 4. Amplitudes of the diurnal and semidiurnal components of the surface pressure variation ($\delta p_s/\bar{p}_s$) measured at the lander sites. Individual data points are shown and represent averages over 5- or 6-sol intervals. The arrows indicate when large increases in the atmospheric opacity were observed at Lander 1.

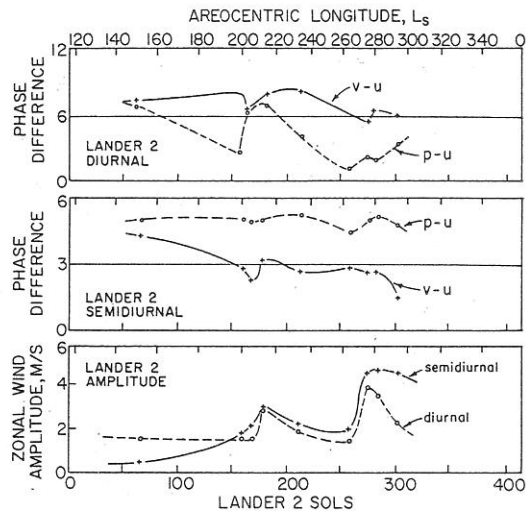

Fig. 6. (Top and middle) Phases of the diurnal and semidiurnal zonal wind component u shown as lag of the west wind maximum relative to the south wind and to the pressure maxima. (Bottom) Amplitudes of the diurnal and semidiurnal components of the zonal wind u measured at Lander 2.

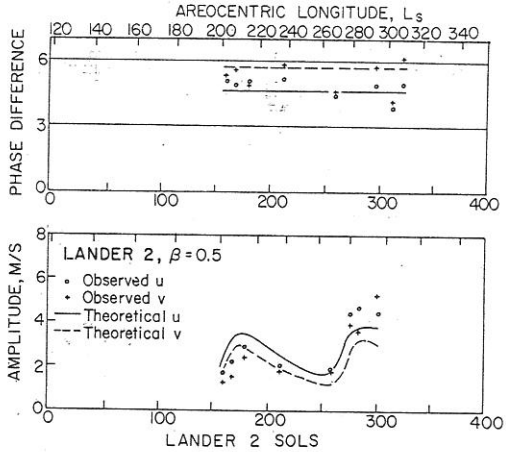

Fig. 7. Comparing (top) phases and (bottom) amplitudes of the semidiurnal zonal wind (u) and meridional wind (v) components observed at Lander 2 with values deduced from the boundary layer model utilizing the observed semidiurnal pressure variations.

viscosity coefficient (assumed constant in the model), z is height, and ∇ is the horizontal gradient operator. Equation (1) is solved under the assumption that

$$\nabla(\ln p_s) = \left[\hat{\mathbf{i}}\left(\frac{is}{a\cos\phi}\right) + a^{-1}\hat{\mathbf{j}}\,\frac{d}{d\phi}\right](\delta p_s/\bar{p}_s) \qquad (2)$$

where $(\delta p_s/\bar{p}_s)$ is the complex amplitude of the relative surface pressure variation (i.e., surface pressure deviation δp_s normalized by the time-averaged surface pressure $\bar{p}_s$), s is the tidal longitudinal wave number ($s = m = 2$ for the propagating semidiurnal tide), a is the planetary radius, ϕ is the latitude, and $\hat{\mathbf{i}}$ and $\hat{\mathbf{j}}$ are unit vectors eastward and northward. The ϕ derivative can be evaluated if the modal structure of the tide is known. This is likely to be quite simple, but we have chosen instead to evaluate the semidiurnal $d(\delta p_s/\bar{p}_s)d\phi$ at Lander 2 by finite differences, using the pressure data from both landers; in so doing we are assuming a very simple latitudinal structure. Equation (1) has the inviscid solution $\mathbf{u}_s = \hat{\mathbf{i}}u_s + \hat{\mathbf{j}}v_s$, where

$$u_s = (1-\nu^2)^{-1}U\left[\nu\,\frac{d}{d\phi}(\delta p_s/\bar{p}_s) - \frac{s}{\cos\phi}(\delta p_s/\bar{p}_s)\right] \qquad (3)$$

$$v_s = (1-\nu^2)^{-1}U\left[\frac{d}{d\phi}(\delta p_s/\bar{p}_s) - \frac{\nu s}{\cos\phi}(\delta p_s/\bar{p}_s)\right] \qquad (4)$$

where $U = RT/a\sigma$ and $\nu = f/\sigma$, with $f = 2\Omega\sin\phi$. The boundary conditions on the viscous solution are taken to be

$$\mathbf{u} \to \mathbf{u}_s \quad \text{as} \quad z \to \infty$$
$$K\frac{\partial \mathbf{u}}{\partial z} = \omega_0\mathbf{u} \quad \text{at} \quad z = 0 \qquad (5)$$

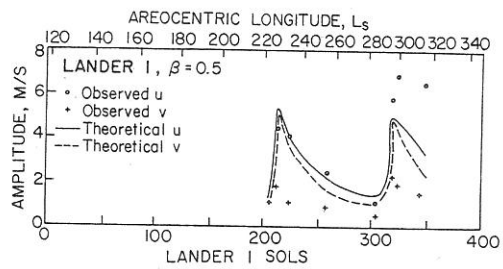

Fig. 8. Same as Figure 7, except for the semidiurnal wind amplitudes at Lander 1.

where ω_0 is a free parameter having dimensions of velocity. Equation (5) is a linearized surface drag law. The solution contains a single dimensionless free parameter, $\beta \equiv (K\sigma)^{1/2}/2\omega_0$. Since ω_0 can be shown to be proportional to the friction velocity u_*, β is a measure of the ratio of the planetary boundary layer depth, proportional to $(K/\sigma)^{1/2}$, to the surface layer length scale u_*/σ. The best fit to the observed amplitude and phase at Lander 2 is obtained using $\beta = \frac{1}{2}$. The resulting fit for the dust storm period is shown in Figure 7. The agreement in amplitude and phase of both semidiurnal wind components is good considering the difficulties of tidal determination at a single site and the simplicity of the theory. There is some indication of larger β values during the second global dust storm, possibly indicative of more rapid upward mixing. Observed tidal amplitudes and phases averaged over the period of Lander 2 sols 157–304 ($L_s \sim 200°$–$300°$) are compared with those calculated in Table 1. We conclude that the semidiurnal oscillations at Lander 2 do correspond to a well-behaved westward propagating semidiurnal tide, as assumed.

The theory has also been applied to Lander 1 data. Agreement with the observed amplitude of the zonal semidiurnal wind is satisfactory (Figure 8), but the observed meridional component is too small. Moreover, the phases are not in agreement with theory: the maximum zonal component appears about 2 hours too early, and the maximum meridional component appears about 5 hours early. We believe that these apparent differences are primarily a consequence of as yet unresolved ambiguities in the determination of wind direction at this site. Nevertheless, it is clear that there is a substantial semidiurnal wind oscillation at Lander 1 which varies with the semidiurnal pressure oscillation and which, at its peak, exceeds that at Lander 2.

A by-product of this model is an empirical determination of the boundary layer scaling appropriate to longer-period motions, such as the synoptic variations described by *Ryan et al.* [1978]. With $\sigma = 0$ the solutions reduce to the classical Ekman layer, and $\beta = \frac{1}{2}$ corresponds to an average turning angle of 28°. An estimate of the effective value of K is also possible. The parameter ω_0 corresponds to $C_D^{1/2}\bar{u}_* = C_D|\bar{\mathbf{u}}|$, where $|\bar{\mathbf{u}}|$

TABLE 1. Comparison of Observed and Calculated Semidiurnal Zone and Meridional Wind Amplitudes and Phases Averaged Over L_s = 200–300

	Lander 1 Average		Lander 2 Average	
	u	v	u	v
Observed	4.23 (3.35)	1.39 (5.36)	3.06 (1.21)	2.75 (0.73)
$\beta = \frac{1}{2}$	3.39 (1.09)	3.06 (0.63)	3.06 (1.39)	2.45 (0.23)
$\beta = 1$	4.81 (0.76)	4.31 (0.45)	4.35 (1.02)	3.38 (1.18)

Amplitudes are in meters per second. Values in parentheses give phase advances (in hours) of u or v in relation to the inviscid solution u_s or v_s, respectively.

is an effective mean value of $|\mathbf{u}|$ and C_D is the drag coefficient at 1.6 m. *Sutton et al.* [1978] have estimated C_D to be of order 0.002–0.003, from which we estimate $\omega_0 \sim 0.01$–0.03 m/s. It follows that $K \sim 1 - 10$ m²/s and the characteristic depth of the Ekman layer, D_e, is equal to $\pi(2K/f)^{1/2} \sim 400$–1200 m. All of these values correspond well with values found in the terrestrial boundary layer under near-neutral stability conditions [e.g., *Businger and Arya,* 1974].

Tidal Simulations Using Simplified Heating Models

In this section we investigate the relationship between the observed surface pressure variations and the strong atmospheric heating produced by airborne dust. Since the observed surface pressure fluctuations are probably planetary in scale [*Hess et al.,* 1977], we use classical atmospheric tidal theory to compute the surface pressure oscillations driven by simple, yet reasonable, distributions of the tidal thermal forcing. These computed oscillations are then compared with the surface pressure variations observed at the two lander sites. Anticipating results shown below, these comparisons indicate that atmospheric heating due to the direct absorption of insolation by airborne dust, which was important even before the first global dust storm observed by Viking occurred, was the overwhelmingly predominant heating source during both of the observed global dust storms. These comparisons further indicate that during the onset of each global dust storm the atmospheric heating rate (per unit mass) had a broad maximum above 10-km altitude but decreased rapidly below. Comparisons of our theoretical tidal fields with the infrared thermal mapper 15-μm observations [*Martin and Kieffer,* 1979] also indicate that there is strong heating above 10 km during global dust storm events.

Tidal Model Description

The tidal model used here is based on the inviscid primitive equations (momentum, continuity, hydrostatic, and thermodynamic) linearized about a basic state atmosphere which is at rest above a topographically uniform surface. The basic state temperature is assumed to be a function only of the nondimensional vertical coordinate $Z = \ln p_0/p$, where p_0 is a constant reference surface pressure ($p_0 \approx \bar{p}_s$). The formulation of the model follows that of *Dickinson and Geller* [1968], except that no gravitational forcing need be included. Also the diabatic heating of the perturbed atmosphere is partitioned here into a periodically varying heating rate per unit mass, J, and a radiative damping represented by a Newtonian cooling coefficient dependent only on Z.

Assuming solutions which are periodic in time and longitude, the five linearized primitive equations can be reduced to one equation which can be solved by separating latitudinal and height dependencies. Thus if the heating rate J and surface pressure ratio $r \equiv \delta p_s/p_0$ are represented as

$$[r, J] = \sum_{m \neq 0} e^{im\Omega t} \sum_s e^{is\lambda} \sum_n [r_n^{m,s}, J_n^{m,s}(Z)]\theta_n^{m,s}(\phi) \qquad (6)$$

where $\theta_n^{m,s}$ is the nth latitudinal, or Hough, mode corresponding to the time and (east) longitudinal periodicities indicated by the integers m and s, respectively, classical tidal theory permits the individual $r_n^{m,s}$ tidal components to be computed once $J_n^{m,s}(Z)$, the basic state temperature $T_0(Z)$, and radiative damping rate $\sigma_R(Z)$ are specified. As in the previous section, $r \approx \delta p_s/\bar{p}_s$ again represents the relative surface pressure variation.

As a first step toward computing global fields of surface pressure variations for comparison with observations at the two lander sites, we have assumed that the heating rate J has the following simple form:

$$J = \alpha_s F_s g p_0^{-1} \sum_{m \neq 0} J^m(Z) e^{im(\Omega t + \lambda)} \sum_n j_n^{m,m} \theta_n^{m,m} \qquad (7)$$

where

$$j_n^{m,m} = (2\pi)^{-1} \int_0^{2\pi} \int_{-\pi/2}^{\pi/2} \cos\eta(\phi, \tilde{t}, \phi_s) e^{-im\tilde{t}} \theta_n^{m,m}(\phi) \, d(\sin\phi) \, d\tilde{t} \qquad (8)$$

is the modal decomposition of the cosine of the solar zenith angle η. F_s is the solar constant at Mars, $g = 3.71$ m s^{-2}, ϕ_s is the subsolar latitude, and $\tilde{t} = \Omega t + \lambda$ is local time expressed in radians. By requiring that

$$\int_0^\infty J^m(Z) e^{-Z} \, dZ = 1 \qquad (9)$$

the vertically integrated volume heating rate of an atmospheric column at the subsolar point is simply

$$\int_0^\infty \rho_0 J(\tilde{t} = 0, \phi_s, z) \, dz = p_0 / g^{-1} \cdot \int_0^\infty e^{-Z} J(\tilde{t} = 0, \phi_s, Z) \, dZ = \alpha_s F_s \qquad (10)$$

where ρ_0 is the basic state density. Thus α_s is the fraction of the total available insolation which appears as atmospheric heating above the subsolar point.

For the present calculations we have assumed $\phi_s = -15°$ and have used 15 Hough functions to represent the diurnal ($m = 1$) tide and five functions to represent the semidiurnal ($m = 2$) component. These modes are listed in Table 2, where their amplitudes at the lander latitudes and the $j_n^{m,m}$ coefficients for $\phi_s = -15°$ are also given. For comparison, equinoctial $j_n^{m,m}$ coefficients are also listed. The large number of diurnal Hough functions reflects the fact that these functions tend to have their largest amplitudes confined to either tropical or extratropical latitudes. Unlike the semidiurnal $\theta_2^{2,2}$ mode, no single diurnal mode has a cosinelike latitudinal variation. As shown by Figure 9, even the 15 diurnal modes used here tend to underestimate the specified diurnal heating rate at the Lander 1 latitude. The neglected modes should have more latitudinal nodes than the functions included in the model; such components of the forcing do not tend to be very effective in producing pressure variations. Therefore we have selected the lowest-order modes (those spanning latitude most smoothly) for both the diurnal and semidiurnal oscillations. The most important diurnal modes are $\theta_1^{1,1}$, $\theta_{-2}^{1,1}$, and $\theta_{-4}^{1,1}$; the first of these can propagate energy vertically so that the amplitudes of its associated temperature and velocity fields tend to grow exponentially with height as energy is propagated into regions of decreasing density [*Chapman and Lindzen,* 1970]. The other two modes cannot propagate energy away, but they are usually large in regions of strong heating. All three modes are symmetric in latitude. Most of the latitudinal asymmetry of the solar heating is represented by the $\theta_{-1}^{1,1}$ mode, which is highly nondivergent and produces little surface pressure variation. This makes the theoretical surface pressure oscillations (but not the tidal temperature field) relatively insensitive to our choice of ϕ_s, the subsolar latitude.

The basic state temperature used here is given by $T_0 = 190K + 56Ke^{-0.4Z}$. The associated lapse rate is steepest at the surface

TABLE 2. The $j_n^{m,m}$ Coefficients of the Model Tidal Heating Computed for $\phi_s = -15°$ and $\phi_s = 0$

(m, n)	$j_n^{m,m}$ $(\phi_s = -15°)$	$j_n^{m,m}$ $(\phi_s = 0)$	$\theta_n^{m,m}$ $(\phi = 22.6°)$	$\theta_n^{m,m}$ $(\phi = 48°)$
(1, 1)	0.079	0.082	−0.287	−0.257
(1, 3)	−0.021	−0.021	−0.171	0.044
(1, 5)	0.010	0.011	0.650	−0.008
(1, 7)	0.006	0.007	1.047	−0.001
(1, −2)	0.250	0.259	0.612	0.930
(1, −4)	−0.075	−0.078	−0.436	−0.159
(1, −6)	−0.038	−0.039	0.341	0.500
(1, −8)	0.023	0.024	0.283	−0.951
(1, −10)	−0.016	−0.016	−0.240	1.110
(1, −12)	−0.014	−0.014	−0.206	0.950
(1, 2)	−0.002	0.	−0.069	0.107
(1,4)	−0.001	0.	−0.415	0.018
(1, −1)	−0.061	0.	0.689	0.962
(1, −3)	−0.017	0.	−0.407	−0.094
(1, −5)	0.002	0.	0.336	−0.511
(2, 2)	0.107	0.113	0.777	0.167
(2, 4)	0.031	0.037	0.679	0.627
(2, 6)	0.015	0.020	−0.942	1.013
(2, 8)	0.008	0.013	−0.069	1.001
(2, 10)	−0.005	−0.009	−0.972	−0.504

Also given are the values of the latitudinal representation functions $\theta_n^{m,m}$ at the lander latitudes. Both the coefficients and functional values are identified by the couplet (m, n).

but does not exceed 50% of the adiabatic lapse rate. The radiative damping time (σ_R^{-1}) increases from 1 day at the surface to 2.5 days at 10 km and then decreases back to 1 day at 60 km, above which it decreases rapidly to 0.2 days at 90 km. This temperature profile and Newtonian cooling coefficient are most appropriate for the mature, or decaying, phase of global dust storms. The temperature profile reflects the dramatic warming and stabilizing of the Martian atmosphere as it becomes dustier [*Conrath et al.*, 1973; *Martin and Kieffer*, 1979]. The radiative damping rate is taken from *Zurek* [1976] and assumes that the atmospheric CO_2 and airborne dust make comparable contributions to the emissivity. These basic state fields and the subsolar latitude have not been varied in the tidal calculations presented here because we wish to isolate the larger effects which occur when the vertical distribution of the heating is substantially altered.

Models of the $J^m(Z)$ profiles are shown in Figure 10. Except for profile $J^m(\mathrm{I})$ the vertical distributions of the diurnal and semidiurnal tidal heating components are identical. For $J^m(\mathrm{I})$ we have assumed that the tidal heating rate varies as exp $[-k_r Z + i(m\tilde{t} - mk_i Z)]$, so that the semidiurnal $(m = 2)$ phase varies twice as fast with height as does the diurnal $(m = 1)$ phase. This faster semidiurnal phase variation coupled with the normalization required by (9) forces the semidiurnal $J^2(\mathrm{I})$ amplitude to be larger than the diurnal $J^1(\mathrm{I})$, as shown in Figure 10. Now, the pressure variation at a point on the surface is produced by the total mass divergence of the atmospheric column above it, and to first order this is determined by the vertically integrated volume heating of the column. Thus for a given $J^m(Z)$ profile, normalized as in (9), the tidal surface pressure amplitude is somewhat insensitive to small changes in the profile. Significant changes do occur when the heating profiles have characteristically different variations with height. The significance of the three profiles shown in Figure 10 will be discussed below.

Simulation of Observed Surface Pressure Ratios

Table 3 compares the computed tidal surface pressure ratios (SPR's) to those observed at the two lander sites during five time intervals. Since the tidal fields are linear in the solar absorption fraction α_s, this factor has been determined by equating the computed and observed amplitudes of the semidiurnal SPR at Lander 1. The Lander 1 semidiurnal component was chosen because it is dominated by a single, fairly broad latitudinal mode $\theta_2^{2,2}$ and thus is somewhat insensitive to details of the basic state parameters (temperature and radiative damping) and of the heating distribution. The numerical values of α_s have been obtained assuming $gF_s/P_0 = 3.9\ \mathrm{W\ kg^{-1}}$.

Profile $J^m(\mathrm{I})$ with its exponentially decaying amplitude and large phase shift with height is designed to simulate tidal thermal forcing produced by convective and radiative transfer from the heated ground. Choosing $k_r = 1.5$ (e folding depth of 6 km) with $k_i = -2$ (heating rate maximum at 6 km lags surface heating maximum by 5 hours) for $J^m(\mathrm{I})$ and setting $\alpha_s = 0.1$ reproduce the semidiurnal SPR observed at the two landers early in the Viking mission, as shown by *Hess et al.* [1977]. As discussed in the earlier study, it is unlikely that this heating rate is produced by the radiative-convective heat flux from the surface alone. This was not unexpected, since even optically thin dust layers can produce significant atmospheric heating rates [*Zurek*, 1978; *Pollack et al.*, 1979], and (dust)

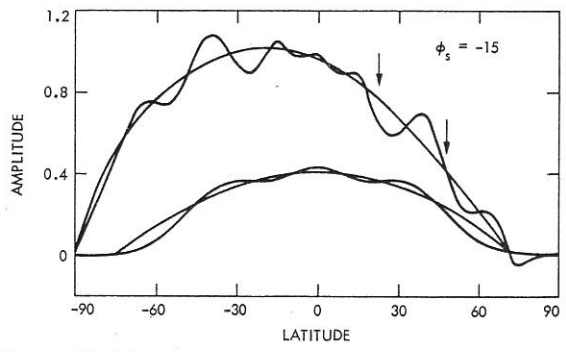

Fig. 9. Model representation of the latitudinal variation of the diurnal and semidiurnal components of cos η, the cosine of the solar zenith angle, when the subsolar latitude is $\phi_s = -15°$. Fifteen Hough functions have been used to represent the diurnal (upper curve) component, and five Hough modes to represent the semidiurnal (lower curve) component. The vertical arrows mark the lander latitudes.

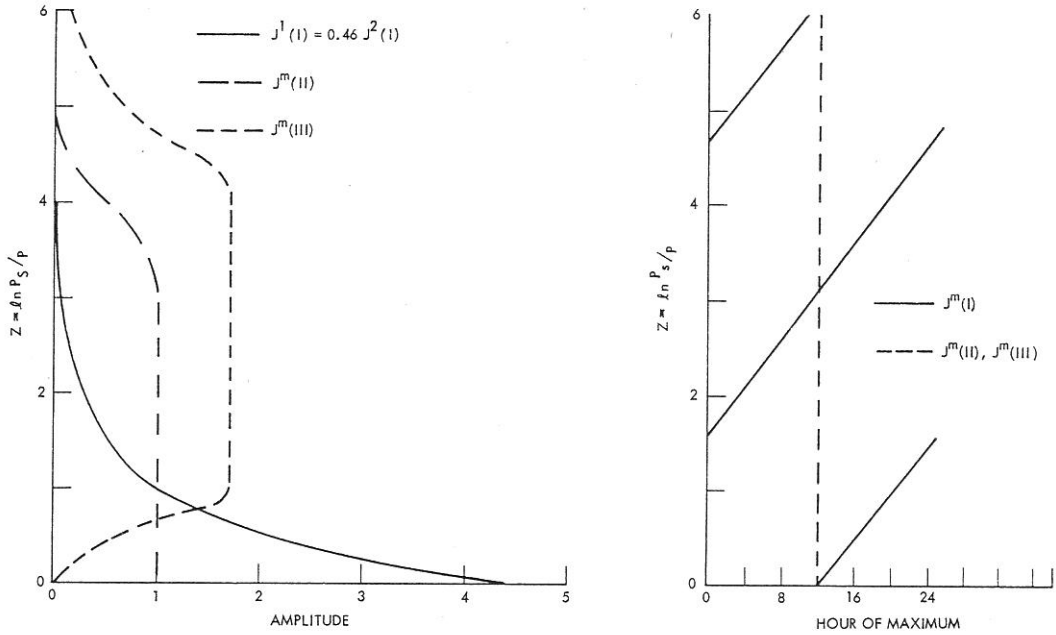

Fig. 10. The amplitude and hour of maximum variation with height for the diurnal ($m = 1$) and semidiurnal ($m = 2$) components of three model profiles for the vertical distribution of the tidal heating rate. $J^m(I)$ simulates the effects of surface heating, while $J^m(II)$ and $J^m(III)$ simulate the results of atmospheric heating by airborne dust. The amplitude curves have been normalized as discussed in the text. Unless otherwise indicated, the same curves have been used for both the diurnal and semidiurnal components.

normal-incident optical depths of $\tau \sim 0.5$ were observed above the landers even during northern midsummer.

Case 1 in Table 3 covers a later period in midsummer which occurs before the appearance of the first global dust storm, but at a time of enhanced surface pressure variation (refer to Figure 4). A solar absorption fraction of $\alpha_s \sim 0.3$ is needed with profile $J^m(I)$ to reproduce the Lander 1 SPR, and most of this large fraction must be due to direct heating of a dusty atmosphere. Somewhat better agreement between the Lander 1 computed and observed SPR can be obtained by using a heating distribution which has a large component which is characteristic of direct heating by airborne dust:

$$J^m(I/II) = 0.6J^m(I) + 0.4\ J^m(II)$$

Although both $J^m(I/II)$ and $J^m(I)$ reproduce the tidal phases observed at Lander 2, they both greatly overestimate the tidal amplitudes there. As the airborne dust heating becomes totally dominant, the heating distribution should approach profile $J^m(II)$ if the dust is fairly uniformly mixed up to 40 km over large regions and if the total extinction optical depth does not significantly exceed $\tau \sim 1$. The uniformity of the $J^m(II)$ profile depends on strong forward scattering by the airborne dust [*Zurek*, 1978] and is suggested by the Mariner 9 observations of the 1971 global dust storm [*Zurek*, 1976]. There was significant dust opacity ($\tau \sim 1$) above both landers just prior to the onset of the first global dust storm observed by Viking [*Pollack et al.*, 1979], and calculations using profile $J^m(II)$ do roughly reproduce the amplitudes of the tidal SPR at both sites, as shown by case 2 in Table 3. The computed hours of maximum, however, are much too early. It should be noted that the good phase agreement produced in case 1 was due to the phase shift of the $J^m(I)$ heating rate. As shown by case 2 (and later in case 4), $J^m(II)$ profile heating yields nearly equal semidiurnal and diurnal SPR amplitudes at Lander 1. Thus in the context of our simplifying assumptions about the heating distribution ($\cos \eta$ variation and same variation with height for all tidal heating components), profile $J^m(II)$ cannot yield the dramatic enhancement of the semidiurnal SPR in relation to the diurnal component which was observed at Lander 1 during the onset of each of the two global dust storms observed by Viking (see Figure 4).

This preferential enhancement of the semidiurnal SPR at Lander 1 is all the more striking during the onset of the first global dust storm, since there is only a modest increase in the semidiurnal component at Lander 2, where the diurnal SPR dominates. As shown in cases 3 and 5, which cover the periods of the onset of the first ($L_s \sim 208°$) and second ($L_s \sim 279°$) global dust storms, respectively, a heating distribution similar to profile $J^m(III)$ can reasonably reproduce the tidal surface pressure variation, particularly the preferential enhancement of the semidiurnal SPR which occurs at the onset of a global dust storm. However, the theoretical diurnal amplitude is much too large for Lander 2, and there are significant phase differences at both sites. If the forcing region of $J^m(III)$ is altered by raising (lowering) the effective bottom of the heating region, the semidiurnal SPR at Lander 1 becomes more (less) enhanced, while the semidiurnal component at Lander 2 remains the same. Examination of the individual $r_n^{2,2}$ tidal components reveals that most of the prominent $r_n^{2,2}$ components are enhanced in amplitude by comparable amounts. However, the higher-order (meaning more latitudinal nodes) modes tend to cancel the contribution of the lowest order mode ($r_2^{2,2}\theta_2^{2,2}$) at Lander 2 but not at Lander 1, where $r_2^{2,2}\theta_2^{2,2}$ predominates. Experimentation using differently shaped profiles, such as $\exp[-(Z - Z_0)^2/\gamma^2]$, indicate that the aspects of profile $J^m(III)$ which are needed to produce the observed semidiurnal SPR enhancement at Lander 1 are that the heating rate practically vanish near the surface and, to a lesser extent, that the region of large heating rate be relatively deep.

As shown by Figure 4, this preferential enhancement of the semidiurnal SPR at Lander 1 gradually disappears during the decaying phases of the two global dust storms. Case 4 of Table

TABLE 3. Comparison of Computed and Observed Tidal Surface Pressure Ratios at the Viking Lander Sites for Selected Periods

Observed/Model		Lander 1 (ϕ = 22.6°)		Lander 2 (ϕ = 48°)	
Lander 1 Sols	L_S, deg	m = 1	m = 2	m = 1	m = 2
		Case 1			
108–112	140	1.99 (7.1)	1.86 (10.5)	0.90 (8.7)	0.39 (10.5)
J (I)	α_s = 0.28*	1.67 (8.0)	1.86 (11.2)	1.26 (9.4)	1.25 (10.9)
J (I/II)	α_s = 0.41*	2.2 (7.3)	1.86 (10.4)	1.73 (8.1)	1.11 (10.4)
		Case 2			
202–207	203	1.18 (9.0)	1.31 (10.3)	0.8 (10.2)	0.7 (09.3)
J (II)	α_s = 0.27*	1.37 (6.0)	1.31 (08.3)	1.3 (06.1)	0.5 (07.7)
		Case 3			
211–216	208	2.7 (6.7)	3.8 (10.1)	2.0 (07.6)	0.9 (09.2)
J (III)	α_s = 0.64*	3.0 (6.3)	3.8 (07.9)	3.4 (06.2)	1.2 (07.0)
		Case 4			
266–270	243	2.1 (6.2)	1.8 (10.7)	1.2 (09.7)	0.9 (09.0)
J (II)	α_s = 0.38*	1.9 (6.0)	1.8 (08.3)	1.8 (06.1)	0.7 (07.7)
		Cases 5			
316–321	279	2.6 (7.7)	4.0 (11.3)	1.2 (10.7)	1.1 (09.0)
J (III)	α_s = 0.67*	3.2 (6.3)	4.0 (07.9)	3.6 (06.2)	1.2 (07.0)

The surface pressure ratios are expressed as $A \cos (mt - mt_h)$, where the tabulated amplitude A are given in percent and the tabulated hours of maximum t_h are given in hours ($\frac{1}{24}$ of the Martian day) and shown in parentheses. The observed data are identified by Lander 1 sols and L_s values. The model results are identified by the heating profile J^m and by the solar absorption fraction used to generate the theoretical fields.

*The theoretical results have been scaled by the α_s value which reproduces the semidiurnal (m = 2) amplitude at Lander 1.

3 shows that 40–50 days after the onset of the first global dust storm, tidal SPR components computed for J^m(II) heating agree quite well with the observed amplitudes, although except for the diurnal phase at Lander 1 there are still significant phase differences. Thus the model calculations indicate that the tidal heating changes rapidly from a J^m(II) distribution to a J^m(III) distribution at the onset of a global dust storm and then slowly back to a J^m(II) distribution as the dust storm decays. The solar absorption fraction jumps to very high values during the onset of both global dust storms. The α_s value for case 4, which covers a phase of the dust storm similar to that observed in 1971 by Mariner 9, suggests that the diurnal thermal forcing, which is about half of the total, represents about 20% of the available insolation. This estimate, which is based on the observed semidiurnal SPR amplitude at Lander 1, agrees with the result *Pirraglia and Conrath* [1974] derived from Mariner 9 temperature data for the 1971 dust storm, and, in fact, case 4 is a nontopographic version of *Zurek*'s [1976] simulation of the diurnal tide observed by Mariner 9.

Comparisons With Infrared Thermal Mapper Data

The Viking temperature data [*Martin and Kieffer*, 1979] can also be used to check our estimates of α_s. Figure 11 shows latitudinal profiles of the diurnal component of the 15-μm atmospheric radiances expressed as equivalent temperatures and computed for cases 1, 3, and 4. These profiles and those of Figure 12 were derived by adding the basic state temperature to the diurnal and semidiurnal temperature oscillations computed for a given latitude by the classical tidal model. These temperatures were converted to vertical column 15-μm radiances by integrating the appropriate Planck function multiplied by the weighting function of the 15-μm channel of the infrared thermal mappers (IRTM) on board the Viking orbiters. These radiances are expressed as equivalent temperature and are then Fourier-analyzed with respect to local time to obtain the diurnal and semidiurnal components at the given latitude. In Figure 11 the theoretical diurnal components of the equivalent temperature for case 1 (L_s = 140°) and for case 4 (L_s = 213°) are compared with diurnal components computed by *Martin and Kieffer* [1979] from Viking IRTM 15-μm observations for L_s values of 120°, 226°, and 290°. The latter two values correspond to periods of 30 days and 16 days, respectively, after the onset of the two observed global dust storms. Case 4 agrees well with the L_s = 226° curve except in the polar region, where the observed amplitude is a factor of 3 larger. The large amplitude observed at high southern latitudes for L_s = 226° does not reappear for L_s = 290°, which represents a similar, though earlier, phase of a global dust storm.

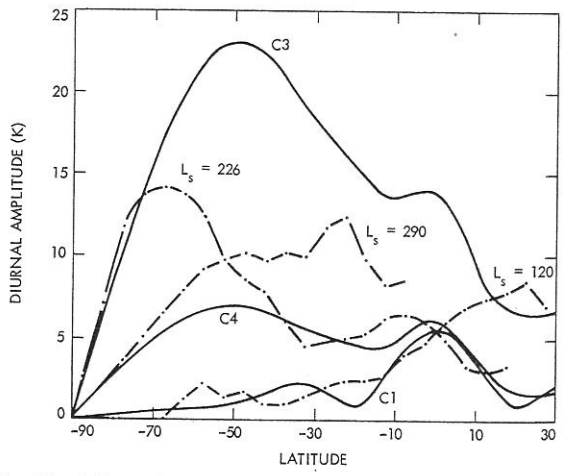

Fig. 11. Theoretical curves (solid lines) for the amplitude of the diurnal component of the equivalent temperature (see text) computed for cases 1, 3, and 4 (denoted C1, C3, and C4, respectively) of Table 3. Also plotted (dashed-dotted curves) are the diurnal amplitudes derived by *Martin and Kieffer* [1979] from the 15-μm radiances observed by the Viking infrared thermal mapper. The observed curves are identified by their L_s values. The L_s values for the theoretical curves are 140, 208, and 243 for C1, C3 and C4, respectively.

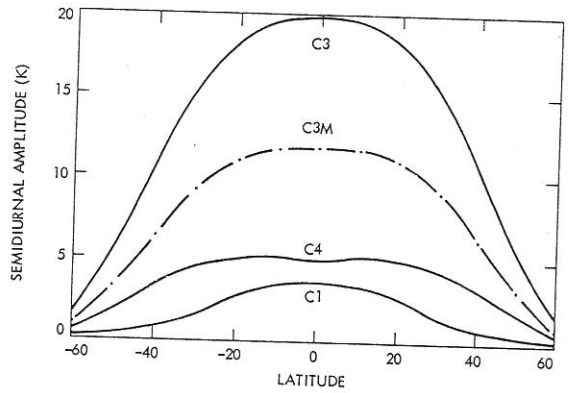

Fig. 12. Theoretical curves for the amplitude of the semidiurnal component of the equivalent temperature computed for cases 1, 3 and 4 of Table 3. Also shown is the theoretical curve (case 3M) which results from using the solar absorption fraction of case 4 with the case 3 heating profile.

Agreement of case 4 with the $L_s = 290°$ curve would require a larger α_s, but this is consistent with the greater opacity observed during the earlier stages of the dust storm. In addition, either model of case 1 agrees well with the $L_s = 120°$ curve south of the equator, although neither continues to rise north of the equator, as indicated by the observations. Considering the simplicity of our tidal heating distributions, this agreement lends credibility to our estimates of the solar absorption fraction, particularly in light of the sensitivity of the equivalent temperatures to the vertical distributions of the heating rate.

This sensitivity is demonstrated in Figure 12, where the semidiurnal components of the equivalent temperature are plotted in cases 1, 3, and 4 as well as for an additional case (denoted 3M) where we have used profile J^m(III) of case 3 with the α_s estimated for case 4. Part of the increase of the semidiurnal component of case 3M relative to case 4 is due to the larger heating rate of J^m(III) relative to J^m(II) in the region extending from 1 to 4 scale heights above the surface, where most of the 15-μm radiance measured by the Viking IRTM originates. However, a comparable increase occurs because, as we saw when computing surface pressure components, profile J^m(III) is more efficient in producing a semidiurnal response than is profile J^m(II). In general, the efficiency of a given heating profile is related to the complex vertical structures of the tidal components being forced. Profile J^m(III), for instance, is not any more efficient than profile J^m(II) when driving diurnal tidal modes. Thus the larger amplitude, relative to case 4, of the diurnal component of the equivalent temperature computed theoretically for the onset of the first global dust storm (curve C3 of Figure 11) is due almost entirely to larger heating rates 10–45 km above the surface and to the large solar absorption fraction used in case 3.

One characteristic of diurnal tidal modes is that those modes which have large amplitudes outside the tropics (e.g., $\theta_{-2}^{1,1}$, $\theta_{-4}^{1,1}$) have vertical structures which decay in amplitude outside layers of strong heating [*Chapman and Lindzen,* 1970; *Zurek,* 1976]. Essentially, these components are dominated by Coriolis forces, and their vertical velocities and temperature oscillations are weak outside active forcing regions. Consequently, the large diurnal variations of the equivalent temperatures observed in mid-latitudes during global dust storms by the Viking IRTM are direct evidence that there is significant heating near 25-km altitude, where the peak of the IRTM 15-μm weighting function occurs, and, by implication, that there is significant dust at these heights during the Martian global dust storms. Indeed, heating by high-level dust may have been exceptionally strong at high southern latitudes when $L_s = 226°$. By the same token, the equivalent temperature measured when $L_s = 120°$ implies that most of the southern hemisphere was relatively clear of dust above 15 km but that there may have been some dust at those altitudes over at least the low latitudes of the northern hemisphere.

Summary of Tidal Model Results

When simulating the surface pressure tidal components observed at the two Viking landers, the tidal model agrees best during periods, including onset, of global dust storm activity. Even then the diurnal amplitude at Lander 2 is greatly overestimated, and there are significant phase differences except for the diurnal tide measured at Lander 1. One particularly puzzling aspect of the observed SPR phases is that the semidiurnal hour of maximum at Lander 1 remains nearly constant at 1030 hours throughout the observation period. Such a phase is reproduced by the model only when the heating rate has a marked phase variation with height, unless the radiative damping rate used here has been greatly underestimated.

At least part of the difficulty of matching the observed diurnal surface pressure variations results from neglecting the effects produced by the large, planetary-scale height variations of the Martian terrain. The surface heat flux excites stronger atmospheric oscillations above elevated terrain, and planetary-scale slopes can dynamically alter atmospheric tidal fields by inducing mass advection and divergence above sloping terrain [*Zurek,* 1976]. Since the topographically modulated surface heat flux is probably important only before the onset of the global dust storms, we would expect better agreement between the model and the observations for global dust storm periods. It is noteworthy that there is little evidence of the topographically induced, resonantly enhanced diurnal Kelvin mode predicted by *Zurek* [1976], probably because the lower Martian atmosphere is stabilized even during northern summer by the presence of airborne dust. Although the semidiurnal tide may be affected by the dynamical effects induced by the planetary-scale variable terrain, no calculation of these effects has yet been carried out.

The simplified heating models used in our calculations probably provide another source of disagreement between theory and observations, particularly in the early part of the Viking mission, when airborne dust may not have been widely or uniformly spread over the planet. Even so, the model calculations do indicate that about 30% of the incoming solar radiation appeared, directly or indirectly, as atmospheric heating just before the onset of the first global dust storm. This fraction doubled to 60% at the onset of each of the two global dust storms. Furthermore, the heating profile which successfully yields the preferential enhancement at Lander 1 of the semidiurnal surface pressure ratio in relation to the diurnal component during the onset of a global dust storm is profile J^m(III) with its elevated heating source. A J^m(III) heating distribution could be produced in one of two ways: (1) the airborne dust is not uniformly mixed with height but is concentrated instead above 10 km or (2) there is so much airborne dust that even if it is uniformly mixed, most of the solar absorption occurs aloft, and little insolation reaches the lowest 10 km of the dusty atmosphere. *Pollack et al.* [1979] have computed the local diurnal temperature range in a dusty Martian atmosphere, and these calculations imply that a vertical solar extinction optical depth of $\tau \gtrsim 3$ is required to produce a heating profile similar to J^m(III). Our own preliminary calcu-

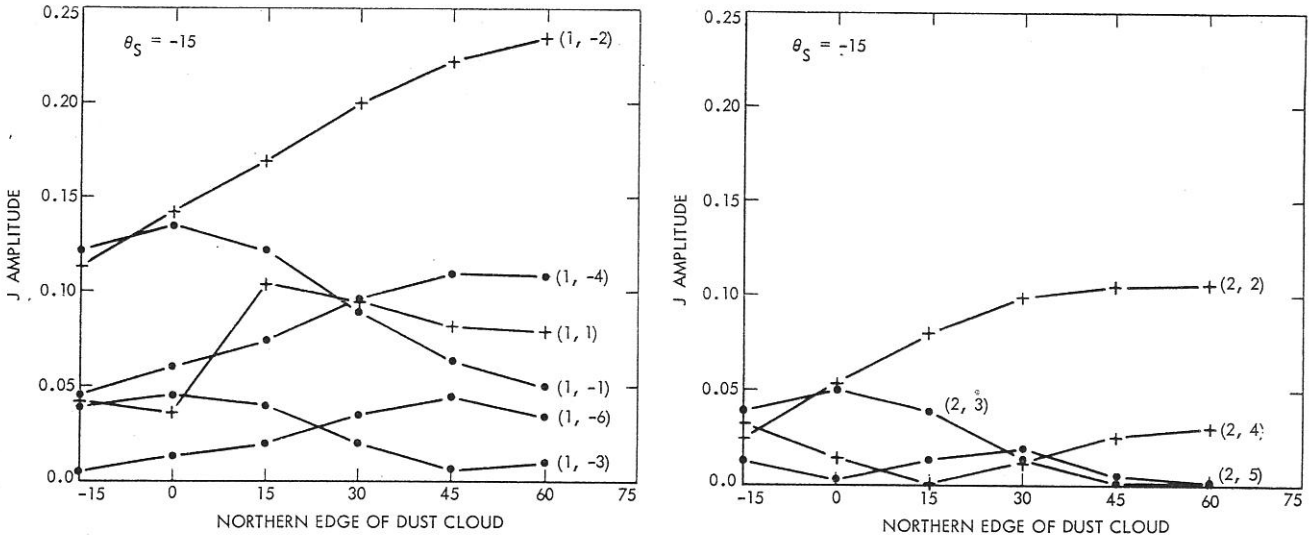

Fig. 13. The $j_n^{m,m}$ coefficients computed for the horizontal distribution of the heating of a longitudinally uniform dust layer extending from latitude $\phi = -60$ to $\phi = \phi_e$ as a function of ϕ_e, the northern edge of the cloud. The curves are computed for a subsolar latitude $\phi_s = -15°$ and are identified by the modal indices (m, n).

lations, using a δ-Eddington radiative code [*Zurek*, 1978] with optical parameters based on the estimates of *Pollack et al.* [1979], give a similar result for the diurnal heating component but suggest that in order for the semidiurnal heating component to have a J^m(III) shape a somewhat larger optical depth ($\tau \gtrsim 5$) is required. *Pollack et al.* [1979] estimate by extrapolation that the optical depths above Lander 1 at the onset of the two global dust storms were 2.9 and 8, respectively. Thus if the Lander 1 opacities are representative of dust spread over vast areas, the dust opacity during the early stages of the second global storm appears to be sufficient to produce the observed semidiurnal predominance at Lander 1, but the opacity observed at Lander 1 during the onset of the first storm may not be quite enough. More detailed calculations of the tidal heating rates in a dusty atmosphere are needed. Of course, there may well be greater dust opacities to the south of Lander 1 during the early stages of the first global dust storm than over the lander itself, since global dust storms tend to originate in the southern hemisphere. Indeed, the fact that the solar absorption fraction was essentially the same during the onset of both global dust storms suggests that the effective optical depth of the widespread dust cloud whose thermal forcing drives the global atmospheric tides was also the same for both events.

In order to estimate the horizontal extent of the dust haze needed to produce global tidal oscillations effectively, the $j_n^{m,m}$ defined by (8) have been recomputed after replacing $\cos \eta$ by $f(\phi) \cos \eta$, where $f(\phi)$ is a step function which is 1 for $-60 \leq \phi \lesssim \phi_e$ and zero elsewhere. This simulates the effect of a longitudinally uniform dust cloud extending from latitude 60°S to latitude ϕ_e. The resulting $j_n^{m,m}$ coefficients for the most important tidal modes are shown in Figure 13 as a function of the northern edge (ϕ_e) of the dust cloud. The largest coefficients ($j_1^{1,1}$, $j_{-2}^{1,1}$, $j_{-4}^{1,1}$, and $j_2^{2,2}$) have attained half of their global ($\phi_e = 60$) values when the dust cloud reaches the equator, 70% when the dust cloud reaches 15°N, and more than 85% if the cloud extends to 30°N. These results imply that airborne dust is spread throughout the Martian low latitudes during a global dust storm. Furthermore, these results suggest that the sharp, nearly simultaneous increase in the amplitudes of the surface pressure oscillations observed at both landers and in the dust opacity measured at Lander 1 at the onset of the global dust storms was produced by the rapid movement of dust from equatorial latitudes past the Lander 1 latitude. A slower movement would have produced a more gradual increase in the observed amplitudes of the surface pressure ratios. This implies that dust was advected at high levels, since winds generally increase with height. Such dust advection aloft would more quickly provide the tidal heating needed above 20 km to produce the observed semidiurnal surface pressure variation at Lander 1 than would raising dust in a stably stratified atmosphere from the surface to the necessary heights. It should be noted that the calculations portrayed in Figure 13 indicate that the dust haze need only cover the Martian low latitudes to produce an observable response in the surface pressure measured at Lander 2; thus it is not necessary for dust opacity above the two landers to increase simultaneously in order for the surface pressure oscillations to amplify simultaneously, as observed during the onset of a global dust storm.

As noted earlier, high-level dust advection could also produce a heating distribution like profile J^m(III) during dust storm onset by concentrating the dust aloft. However, the observed preferential enhancement of the semidiurnal tide at Lander 1 indicates that profile J^m(III) may have characterized the tidal heating distribution for many days after dust storm onset, and it is not clear how a high-level concentration of strongly absorbing dust could maintain itself for 10–20 days against the intense convective mixing which appears to occur in the expanding dust cloud [*Briggs et al.*, 1979]. Even so, both dust advection aloft and attenuation of heating rates due to large dust opacities may be important during the onset of a global dust storm. For instance, a J^m(III) heating distribution may be initially formed by high-level dust advection from dust centers in the southern hemisphere. This would immediately enhance tidal winds near the surface and enable dust to be raised over large areas in northern as well as southern latitudes. When added to dust already distributed aloft, the newly raised dust could then produce a large enough opacity to maintain the J^m(III) distribution even as the dust is mixed more uniformly with height. As discussed in our concluding section, this may be one of several mechanisms important for the development of global dust storms.

DISCUSSION: DUST STORM GENERATION AND DECAY MECHANISMS

Our main conclusions are the following: (1) atmospheric dust opacity and global thermally driven tides are intimately coupled, (2) atmospheric heating by airborne dust is important even before the onset of the first global dust storm, (3) the global spread of dust occurs rapidly, with onset marked by a jump in global tides and the concurrent advection of airborne dust past Lander 1, (4) the semidiurnal tide is quite strong and is comparable at low latitudes to the diurnal component, both before and during global dust storms, (5) the semidiurnal surface pressure variation and its associated wind field dominate their diurnal counterparts during the peak stages of the global storms, when both tides are greatly enhanced, and (6) the preferential enhancement of the semidiurnal surface pressure oscillation at Lander 1 at the onset of a global dust storm can be produced by a heating distribution which has a broad maximum above 10-km altitude, below which it rapidly decreases and whose total heating represents more than half of the available insolation.

These conclusions are relevant to the problem of global dust storm generation and decay. *Leovy et al.* [1973*b*] suggested that the thermally driven meridional circulation and diurnal tides were important factors for dust storm genesis. They proposed that both of these global wind systems would be enhanced prior to the main storm onset as a result of heating in an increasingly dusty atmosphere. This prior increase in dust would occur, it was argued, largely as a consequence of local dust storms along the dynamically active periphery of the south polar cap. In an alternative model, *Gierasch and Goody* [1973] proposed that the global dust storms arise from expansion of one or more 'dusty hurricanes.' These are postulated local storms in which differential heating due to absorption of solar radiation in the dust cloud plays a driving dynamical role analogous to that of latent heat release in terrestrial hurricanes. Gierasch and Goody also emphasized the significant potential of topographically generated wind systems in global dust storm generation. Their model contains a dust storm self-destruct mechanism: once the dust becomes global, the radiatively generated temperature gradients which help to drive it disappear.

The Viking data suggest that each of these mechanisms plays a role. The increase in opacity and in tidal activity prior to dust storm onset, which was postulated by *Leovy et al.* [1973*b*], has been observed. There is also a striking tendency for the local dust storms, which appear to be responsible for this precursor opacity, to occur in two regions; along the edge of the receding south polar cap, and in the upland region of Sinai Planum and Solis Planum, near 20°S and 120°W [*Peterfreund and Kieffer,* 1979]. The latter is one of the regions in which the maximum diurnal tidal winds are expected [*Conrath,* 1975; *Zurek,* 1976]. On the other hand, the orbiter images showing the early stages of the 1977 dust storm indicate a major topographic influence. At its onset the dust being raised from the surface was strongly constrained by the topography of the Claritas Fossae region (near 40°S, 110°W), and it appeared to be driven by winds which had a strong, topographically generated thermal component [*Briggs et al.,* 1979]. Moreover, many of the local and regional-scale dust clouds which have been observed show intense convective activity with cumuliform turrets reaching 15 km or more, indicating the important role played by dust heating in these individual storms [*Briggs et al.,* 1979; *Briggs and Leovy,* 1974]. After the onset of the global storms the global meridional circulation appears to be important. This is indicated by the prevalent northeasterly winds at both sites and the buildup of pressure north of Lander 2, especially after the onset of the second storm. The strongest winds at both landers were northeasterly; this is the direction of the windblown features at the Lander 1 site and of the global streak pattern in the latitude range of the landers [*Sagan et al.,* 1973, 1977; *Ward,* 1978]. It is also the direction expected for a thermally driven circulation with the major heat source located south of the landers. Thus precursor dust storm activity, tides, meridional winds, topographic winds, and winds generated by differential heating due to the dust clouds all appear to be factors in storm generation.

The Viking data also show that rapid spread of dust away from the centers of storm activity and high-level heating through a deep atmospheric layer are characteristics of the global storms. One of the unique features of these storms seems to be that the dust is transported to high enough levels that it can be rapidly spread over the planet. This requires that the centers of dust-raising activity be large enough, intense enough, and sufficiently strongly heated that large quantities of dust can be lifted to 2 scale heights or more. One of the most remarkable features of the observed global storms is the height to which the dust is raised over most of the planet [*Anderson and Leovy,* 1978]. At altitudes of 20 km or more, transport by the mean meridional circulation and by atmospheric tides can provide very rapid transport over much of the planet. In a steady state situation these two components would tend to compensate each other, but the actual surge of dust outward from its regional source probably results from the intensification of both the mean and tidal meridional circulations by the diabatic heating of the spreading dust.

Dust storm decay, which seems to begin almost immediately after storm onset, may also involve several mechanisms. However, if dust transport to high altitude is an integral component of the global storms, the dramatic increase in static stability which accompanies storm onset [*Conrath et al.,* 1973; *Martin and Kieffer,* 1979] would act very effectively to suppress further vertical motion of the dust and could prevent it from rising to altitudes at which rapid spread over the planet is possible. Dust raised to high levels during the onset phase of a storm would then gradually fall out or, as suggested by *Pollack et al.* [1979], would be transported to the winter polar region, where fallout could be accelerated by CO_2 condensation around the dust particles.

Acknowledgments. C. Leovy gratefully acknowledges valuable discussions and assistance with Viking data processing by his colleagues James Tillman and Jeff Barnes. R. Zurek thanks Clara Bowie for her expeditious typing of a difficult manuscript. This work was supported by the Planetary Atmospheres program of NASA under contract NAS7-100 and by Viking Project grant NASI-9464.

REFERENCES

Anderson, E. H., and C. B. Leovy, Mariner 9 television limb observation of dust and ice hazes on Mars, *J. Atmos. Sci., 35,* 723–734, 1978.

Briggs, G. A., and C. B. Leovy, Mariner 9 observations of Mars' north polar hood, *Bull. Amer. Meteorol. Soc., 55,* 278–296, 1974.

Briggs, G. A., W. A. Baum, and J. Barnes, Viking orbiter imaging observations of dust in the Martian atmosphere, *J. Geophys. Res., 84,* this issue, 1979.

Businger, J. A., and S. P. S. Arya, Height of the mixed layer in the stably stratified planetary boundary layer, *Advanc. Geophys., 18A,* 73–92, 1974.

Capen, F. C., and L. J. Martin, Survey of Martian yellow storms, *Bull. Amer. Astron. Soc., 4,* 374, 1972.

Chapman, S., and R. S. Lindzen, *Atmospheric Tides,* 200 pp., Gordon and Breach, New York, 1970.

Conrath, B. J., Thermal structure of the Martian atmosphere during dissipation of the dust storm of 1971, *Icarus, 24,* 36–46, 1975.

Conrath, B. J., R. Curran, R. Hanel, V. Kunde, W. Maguire, J. Pearl, J. Pirraglia, J. Welker, and T. Burke, Atmospheric and surface properties of Mars obtained by infrared spectroscopy on Mariner 9, *J. Geophys. Res., 78,* 4267–4278, 1973.

Dickinson, R. E., and M. A. Geller, A generalization of 'tidal theory with Newtonian cooling,' *J. Atmos. Sci., 25,* 932–933, 1968.

Gierasch, P. J., and R. M. Goody, The effect of dust on the temperature of the Martian atmosphere, *J. Atmos. Sci., 29,* 400–402, 1972.

Gierasch, P. J., and R. M. Goody, A model of a Martian great dust storm, *J. Atmos. Sci., 30,* 169–179, 1973.

Hess, S. L., R. M. Henry, C. B. Leovy, J. A. Ryan, and J. E. Tillman, Meteorological results from the surface of Mars: Viking 1 and 2, *J. Geophys. Res., 82,* 4559–4574, 1977.

Leovy, C. B., G. A. Briggs, and B. A. Smith, Mars atmosphere during the Mariner 9 extended mission: Television results, *J. Geophys. Res., 78,* 4252–4266, 1973*a*.

Leovy, C. B., R. W. Zurek, and J. B. Pollack, Mechanisms for Mars dust storms, *J. Atmos. Sci., 30,* 749–762, 1973*b*.

Martin, T. Z., and H. Kieffer, Thermal infrared properties of the Martian atmosphere, 2, The 15-μm band measurements, *J. Geophys. Res., 84,* this issue, 1979.

Masursky, H., et al., Mariner 9 television reconnaisance of Mars and its satellites: Preliminary results, *Science, 175,* 294–304, 1972.

Peterfreund, A. R., and H. H. Kieffer, Thermal infrared properties of the Martian atmosphere, 3, Local dust clouds, *J. Geophys. Res., 84,* this issue, 1979.

Pirraglia, J. A., and B. J. Conrath, Martian tidal pressure and wind fields obtained from the Mariner 9 infrared spectroscopy experiment, *J. Atmos. Sci., 31,* 318–329, 1974.

Pollack, J. B., D. S. Colburn, R. Kahn, J. Hunter, W. Van Camp, C. E. Carlston, and M. R. Wolfe, Properties of aerosols in the Martian atmosphere, as inferred from Viking lander imaging data, *J. Geophys. Res., 82,* 4479–4496, 1977.

Pollack, J. B., D. S. Colburn, F. M. Flasar, C. E. Carlston, D. Pidek, and R. Kahn, Properties and effects of dust particles suspended in the Martian atmosphere, *J. Geophys. Res., 84,* this issue, 1979.

Ryan, J. A., and R. M. Henry, Mars atmospheric phenomena during major dust storms, *J. Geophys. Res., 84,* this issue, 1979.

Ryan, J. A., S. L. Hess, R. M. Henry, C. B. Leovy, J. E. Tillman, and C. Walcek, Mars meteorology: Three seasons at the surface, *Geophys. Res. Lett., 5*(8), 510, 1978.

Sagan, C., J. Veverka, P. Fox, R. Dubisch, R. French, P. Gierasch, L. Quam, J. Lederberg, E. Levinthal, R. Tucker, and B. Eross, Variable features on Mars, 2, Mariner 9 global results, *J. Geophys. Res., 78,* 4163–4196, 1973.

Sagan, C., D. Pieri, P. Fox, R. E. Arvidson, and E. A. Guinness, Particle motion on Mars inferred from the Viking lander cameras, *J. Geophys. Res., 82,* 4430–4438, 1977.

Sutton, J. L., C. B. Leovy, and J. E. Tillman, Diurnal variations of the Martian surface layer meteorological parameters during the first 45 sols at two Viking lander sites, *J. Atmos. Sci., 35,* 2346–2355, 1978.

Ward, A. W., Jr., Windforms and wind trends on Mars: An evaluation of Martian surficial geology from Mariner 9 and Viking spacecraft television images, Ph.D. thesis, Dep. of Geol. Sci., Univ. of Wash., Seattle, 1978.

Zurek, R. W., Diurnal tide in the Martian atmosphere, *J. Atmos. Sci., 33,* 321–337, 1976.

Zurek, R. W., Solar heating of the Martian dusty atmosphere, *Icarus, 35,* 196–208, 1978.

(Received July 18, 1978;
accepted October 12, 1978.)